

Article

Piezoelectric Transducers: Complete Electromechanical Model with Parameter Extraction

Michael L. Isaf * and Gabriel A. Rincón-Mora

School of Electrical and Computer Engineering, Georgia Institute of Technology, Atlanta, GA 30332, USA; rincón-mora@gatech.edu

* Correspondence: misaf@gatech.edu

Abstract: This paper presents a complete electromechanical (EM) model of piezoelectric transducers (PTs) independent of high or low coupling assumptions, vibration conditions, and geometry. The PT's spring stiffness is modeled as part of the domain coupling transformer, and the piezoelectric EM coupling coefficient is modeled explicitly as a split inductor transformer. This separates the coupling coefficient from the coefficient used for conversion between mechanical and electrical domains, providing a more insightful understanding of the energy transfers occurring within a PT and allowing for analysis not previously possible. This also illustrates the role the PT's spring plays in EM energy conversion. The model is analyzed and discussed from a circuits and energy harvesting perspective. Coupling between domains and how loading affects coupled energy are examined. Moreover, simple methods for experimentally extracting model parameters, including the coupling coefficient, are provided to empower engineers to quickly and easily integrate PTs in SPICE simulations for the rapid and improved development of PT interface circuits. The model and parameter extractions are validated by comparing them to the measured response of a physical cantilever-style PT excited by regular and irregular vibrations. In most cases, less than a 5–10% error between measured and simulated responses is observed.

Keywords: coupling coefficient; electromechanical model; energy harvesting; equivalent impedance; irregular and regular vibrations; mode of vibration; Norton and Thevenin equivalent; parameter extraction; piezoelectric



Citation: Isaf, M.L.; Rincón-Mora, G.A. Piezoelectric Transducers: Complete Electromechanical Model with Parameter Extraction. *Sensors* **2024**, *24*, 4367. <https://doi.org/10.3390/s24134367>

Academic Editor: Tian-Bing Xu

Received: 25 May 2024

Revised: 27 June 2024

Accepted: 2 July 2024

Published: 5 July 2024



Copyright: © 2024 by the authors. Licensee MDPI, Basel, Switzerland. This article is an open access article distributed under the terms and conditions of the Creative Commons Attribution (CC BY) license (<https://creativecommons.org/licenses/by/4.0/>).

1. Introduction

To increase ease of use, practicality, and desirability, many devices, especially in the Internet of Things, require minimal maintenance power methods. Numerous mechanical, biomedical, and civil systems produce vibrations, and piezoelectric transducers (PTs), with their high energy densities and off-the-shelf availability, can effectively and easily tap into this energy source [1–5].

PTs convert mechanical energy, in the form of motion or vibration, to electrical energy that can be harvested to charge a battery, v_B , and power a microsystem, as illustrated in Figure 1. Ultimately, maximizing the harvester's output power, P_O , is most important, but to do so, an understanding of how the PT delivers power, P_{PZ} , is required [6–8].

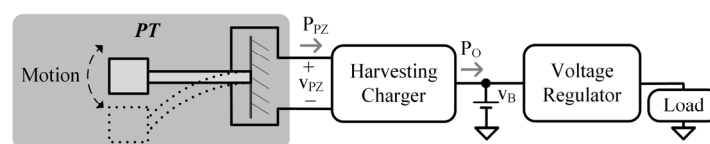


Figure 1. Piezoelectric-powered energy-harvesting system.

Transducers are not ideal energy sources, so a source model which accurately represents source impedances and energy conversions is important to design energy harvesting

systems well. In a PT, an understanding of how mechanical motion produces electrical energy, electrical loading affects output power, and energy couples between domains is necessary when designing harvesters effectively for specific motion inputs. This requires an insightful PT model with parameters that can effectively approximate the physical device.

The model shown in [9–11] provides a circuit representation of both the mechanical and electrical domains of a PT, along with a method of coupling between the two to capture loading effects. However, the transformer’s coupling coefficient and turns ratio are combined into a single coefficient, which removes insight and analysis potential and can lead to inaccuracies. It is also known that PTs exhibit a dual resonance (parallel and series) behavior that is not captured [12–15]. In other words, that model does not adequately model PT output impedance. Moreover, mechanical engineers often use mechanical methods, material properties, and/or finite element analysis to determine model parameters, which may be inaccessible to many electrical engineers [9–11].

Other models exclude the mechanical domain and approximate i_{pZ} to be proportional to the PT’s tip velocity (for cantilevered PTs). In these cases, the PT is assumed to be very weakly coupled, so the electrical load is said to have negligible effect on the PT’s motion [1,4,7,16–20]. It is not clear though, what constitutes weak coupling or how a PT is determined to be weakly coupled. DC-DC converters using PTs, such as those described in [12–15], require good impedance models for accurate converter and control design. Such applications often use the Van Dyke model, but this model is lumped, leading to potential error in converter design and PT impedance understanding, and its derivation could be expanded on [21]. This model is typically used for “strongly coupled” PTs, which poses similar ambiguity as before.

This paper presents a complete electromechanical (EM) model for PTs independent of strong or weak coupling assumptions, vibration conditions, and transducer geometries, making it generally applicable to many PT types, sizes, and applications. Because the model details enable insight into the power and energy transfers and losses occurring within PTs, it is particularly useful in energy harvesting contexts. PT impedances and resonances are also analyzed and discussed, exhibiting the model’s use for PT resonators. The model is also reduced to its Norton and Thevenin equivalents, which are applicable in all coupling contexts. Simple methods for experimentally extracting model parameters are presented and discussed to empower designers to quickly and easily integrate PTs in SPICE simulations for the rapid and improved development of PT interface circuits.

2. Complete Electromechanical Model

The complete EM model of a PT presented in this section strives to capture and distinguish between the aspects of the PT responsible for motion, energy capture, domain conversion, and electrical behavior. Equivalents of the complete model are also presented for ease of use. The model is developed using a cantilever style PT but is generally valid.

2.1. Complete Model

In Figure 2, the PT mass, M_T , has kinetic energy when in motion with velocity, v_T . Similarly, a capacitor has energy when a voltage develops across it. So, M_T can be modeled as a capacitor, where $C_T \equiv M_T$ [kg], and the mass’s velocity, in [m/s], is analogous to the capacitor voltage, v_T [22,23]:

$$E_{KE} = 0.5M_T v_T^2 \equiv E_C = 0.5C_T v_T^2. \quad (1)$$

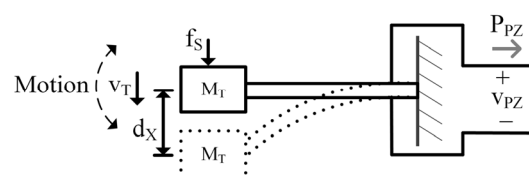


Figure 2. Diagram representing PT motion.

A mass moves if force is applied to it and a capacitor develops a voltage if current is applied to it. Since v_T represents both voltage and velocity, its time derivative can represent the transducer’s acceleration, a_T , and since $C_T \equiv M_T$, the current, i_S , into C_T is analogous to an applied mechanical force, f_S , on M_T in units of $[kg(m/s^2)]$ or $[N]$. Therefore,

$$i_S = C_T \left(\frac{dv_T}{dt} \right) \equiv M_T a_T = f_S. \tag{2}$$

Springs store potential energy when compressed (or bent for a cantilever) a distance, d_X , from rest. Inductors store energy when magnetized by ϕ_L , thus an inductor can model a spring with spring constant, K_T :

$$E_{PE} = 0.5K_T d_X^2 \equiv E_L = 0.5 \left(\frac{1}{L_T} \right) \phi_L^2 = 0.5L_T i_{LT}^2, \tag{3}$$

where L_T is inversely equal to K_T $[N/m]$ and i_{LT} represents force applied by the spring.

Frictional sources, such as air resistance, dissipate energy and dampen mechanical motion in the same way resistors dissipate energy in electrical systems:

$$D_T = \frac{f_D}{v_T} \equiv G_T = \frac{1}{R_T} = \frac{i_R}{v_T}. \tag{4}$$

Mechanical dampers, D_T $[kg/s]$, apply a force, f_D , in response to motion, v_T . So, in keeping with the convention established above, mechanical damping, D_T , is analogous to the inverse of resistance, R_T , (i.e., conductance, G_T) where i_R is the current through the resistor and v_T is the voltage across it, as seen in (4) [24].

The LC circuit analogous to the spring mass system described above will have the same resonant frequency, f_R :

$$f_R = \frac{1}{2\pi\sqrt{\frac{M_T}{K_T}}} \equiv f_{LC} = \frac{1}{2\pi\sqrt{L_T C_T}}. \tag{5}$$

The energy transfer between the mechanical domain (MD) and electrical domain (ED) of a PT is typically modeled with a transformer [9–11]. Since PTs and piezoelectric (PZ) materials are not capable of capturing all mechanical energy present for conversion to the ED, a coupling coefficient, k_{CL} , exists:

$$k_{CL} \equiv \frac{L_{TC}}{L_T} = \frac{L_{TC}}{L_{T0} + L_{TC}} = \frac{C_{LC}'}{C_L'} = \frac{C_{LC}'}{C_{L0}' + C_{LC}'} \leq 1. \tag{6}$$

k_{CL} is intrinsic to the PT and is what makes a PT a PT. It represents the inherent strength of the connection between domains—the larger k_{CL} , the better the connection. k_{CL} can only be between 0 and 1, inclusive. A k_{CL} of 0 corresponds to a material that is not piezoelectric as this implies no coupling exists between the ED and MD [1,25].

Figure 3 is the complete EM PT model with the MD modeled on the left. In the state of the art (SoA), k_{CL} is often lumped in with the transformer [9–11]. In Figure 3, however, it is represented as the ratio between L_{TC} and L_T , as (6) shows, where L_{TC} is the portion of L_T that perfectly couples with the ED. k_{CL} can also be thought of as the percentage of v_T that couples to current in the ED, i_{EC} , when the output is shorted.

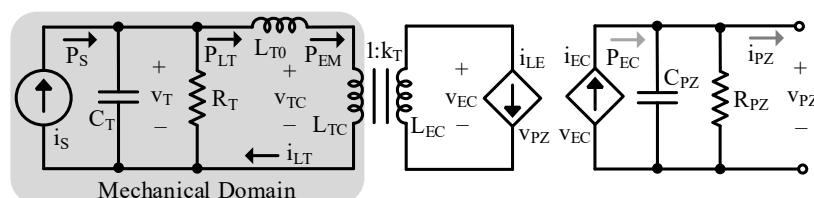


Figure 3. Complete electromechanical PT model.

In a conventional transformer, voltage on the secondary is a multiple of primary voltage by a factor of the turns ratio, k_T [26]. Of course, there are no “turns” in a PT, so k_T

is referred to here as the translation coefficient, representing the conversion between the MD (force/velocity) and the ED (current/voltage):

$$k_T \equiv \frac{v_{EC}}{v_{TC}} = \sqrt{\frac{L_{EC}}{L_{TC}}}. \quad (7)$$

In a PT, it is generally accepted that velocity begets current, i_{EC} , so the two dependent current sources are used in conjunction with the transformer to couple v_T to i_{EC} [1,4,7,9,16–20]. The dependent current sources perform a voltage-to-current conversion which reciprocates impedances (i.e., resistance to conductance, inductance to capacitance, etc.) and dividers (i.e., voltage dividers to current dividers and vice versa). Lastly, C_{PZ} models the PT's ability to store electrical energy, and R_{PZ} models leakage. C_{PZ} is often dominated by the capacitance that exists between the PT's electrodes [10,27]. The parameters in Figure 3 are the most fundamental to the model, so they have been italicized in the text to assist the reader in tracking them throughout the paper.

Presenting the model as it is described here (as opposed to representing mass as inductance and stiffness as capacitance as is often performed in the SoA, such as in [9–11]) is vital for a few reasons. First, it allows the inductor to be incorporated into the transformer, illustrating the role the PT stiffness plays in domain coupling/energy transfer by representing the spring as the medium for EM conversion [9]. It also enables explicit visualization of the transformer coupling coefficient by using split inductors to clearly show that only a fraction of the velocity, v_{TC} , (i.e., mechanical energy) couples to the ED. Lastly, by using split inductors to represent transformer coupling, the transformer turns ratio can also be explicitly defined. Separating k_{CL} from k_T is important because if the coupling coefficient were lumped in with k_T , it would be incorrectly applied to all impedance translations, as will be shown in Section 2.2. It also introduces the dual resonance behavior into the model, as will be shown in Section 2.3.

This model makes the same assumptions about PTs as those used in and accepted by the SoA, such as in [9–20]. These assumptions are: (1) A PT which behaves as a spring-mass-damper system in the mechanical domain is used; (2) Mechanical velocity is in phase with PT short circuit current; (3) The PT's electrical domain is predominately capacitive. The transformer and split inductors are methods for fundamentally representing conversion and coupling between domains—regardless of its geometry and material, a PT converts energy between domains and only some fraction of energy couples. Therefore, this model and the following analysis can be applied to any PT that satisfies the three assumptions, which encompasses the majority of PTs used in energy harvesting and many PTs used as resonators [1,9–20].

2.2. Electrical Model

To simplify analysis, it is helpful to use a circuit equivalent to Figure 3 which does not include the transformer or dependent sources. The MD impedances, Z_T , can be referred to the ED, Z_Z' , using typical transformer techniques as seen in [26]:

$$Z_Z' \equiv Z_T k_T^2. \quad (8)$$

As mentioned above, the dependent current sources reciprocate impedances and dividers.

The results of the above translations are shown in Figure 4. By representing the model this way, coupling between the MD and ED is modeled with a coupling capacitor, C_{LC}' , and a leakage capacitor, C_{L0}' , which are related to k_{CL} by (6). Note that if k_{CL} and k_T were lumped, all translated impedances, instead of just L_{T0} and L_{TC} , would be affected by k_{CL} . When k_{CL} is greater than 50%, C_{LC}' is larger than C_{L0}' , so more than half the mechanical energy present can couple to the ED. When less than 50%, the opposite is true.

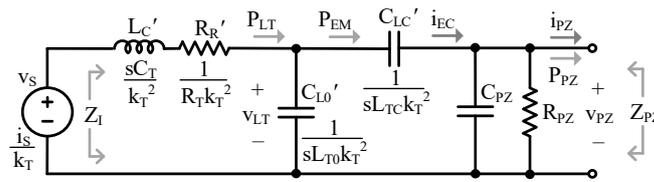


Figure 4. Electrical model.

2.3. Lumped Electrical Model

Reducing the model to its Norton and/or Thevenin equivalent, shown in Figure 5, is helpful for simple and easy application. To create these equivalent circuits, an understanding of the PT's output impedance, Z_{PZ} , is required.

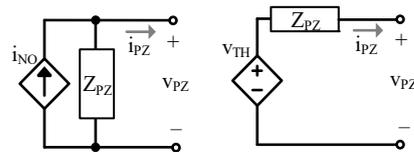


Figure 5. Norton and Thevenin equivalents.

Z_{PZ} can be determined by shorting v_s in Figure 4 and evaluating impedance when looking left from v_{PZ} [28]:

$$\begin{aligned}
 Z_{PZ} &= R_{PZ} \left\| \frac{1}{sC_{PZ}} \right\| \left\{ \frac{1}{k_T^2} \left\{ \frac{1}{sL_{TC}} + \left[\frac{1}{sL_{T0}} \right] \left\| \left(\frac{1}{R_T} + sC_T \right) \right\| \right\} \right\} \\
 &= R_{PZ} \left\| \frac{1}{sC_{PZ}} \right\| \left\{ \frac{1}{sC_{LC'}} + \left[\frac{1}{sC_{L0'}} \right] \left\| (R_{R'} + sL_{C'}) \right\| \right\} \\
 &= R_{PZ} \left\| \left[\frac{1}{s(C_{LC'} + C_{PZ})} \right] \left[\frac{\left(\frac{s}{2\pi f_R} \right)^2 + \frac{1}{Q_R} \left(\frac{s}{2\pi f_R} \right) + 1}{\left(\frac{s}{2\pi f_R'} \right)^2 + \frac{1}{Q_R'} \left(\frac{s}{2\pi f_R'} \right) + 1} \right] \right\} \\
 &= \left(\frac{R_{PZ}}{1 + \frac{s}{2\pi f_{PX}}} \right) \left[\frac{\left(\frac{s}{2\pi f_R} \right)^2 + \frac{1}{Q_R} \left(\frac{s}{2\pi f_R} \right) + 1}{\left(\frac{s}{2\pi f_R'} \right)^2 + \frac{1}{Q_R'} \left(\frac{s}{2\pi f_R'} \right) + 1} \right].
 \end{aligned} \tag{9}$$

At very low frequencies, $L_{C'}$ is effectively a short relative to $C_{LC'}$ and $C_{L0'}$. As frequency increases though, its impedance will no longer be negligible, and it will interact with $C_{LC'}$ and $C_{L0'}$, resulting in a mechanical, series resonance, f_R , given in (5). The quality factor, Q_R , at f_R is:

$$Q_R = \frac{1}{R_{R'}} \sqrt{\frac{L_{C'}}{C_{L'}}} = R_T \sqrt{\frac{C_T}{L_T}}. \tag{10}$$

Above, f_R , $L_{C'}$ shunts the surrounding capacitors until frequency increases enough for $L_{C'}$ to effectively open relative to them, resulting in an EM, parallel resonance, f_R' :

$$\begin{aligned}
 f_R' &= \frac{1}{2\pi \sqrt{L_{C'} [C_{L0'} + (C_{LC'} \oplus C_{PZ})]}} \\
 &= \frac{1}{2\pi \sqrt{C_T \left[L_{T0} + \left(L_{TC} \left\| \frac{C_{PZ}}{k_T^2} \right\| \right) \right]}} \\
 &= \frac{f_R}{\sqrt{(1 - k_{CL}) + \frac{k_{CL} C_{PZ}}{L_{TC} k_T^2 + C_{PZ}}}} \equiv f_R k_{F'},
 \end{aligned} \tag{11}$$

with a quality factor, Q_R' , of

$$Q_R' = \frac{1}{R_{R'}} \sqrt{\frac{L_{C'}}{C_{L0'} + (C_{LC'} \oplus C_{PZ})}} = R_T \sqrt{\frac{C_T}{L_{T0} + \left(L_{TC} \left\| \frac{C_{PZ}}{k_T^2} \right\| \right)}}. \tag{12}$$

In this paper, “ \oplus ” indicates the electrical series combination of capacitors (which are mathematically parallel).

Below f_R , L_C' shorts, so C_{PZ} and C_{L_C}' dominate:

$$Z_{PZ}|_{p_{PZ} < f_0 < f_R} \approx \frac{1}{sC_{LF}} = \frac{1}{s(C_{L_C}' + C_{PZ})}, \quad (13)$$

until frequency drops low enough for them to be open relative to R_{PZ} , which occurs at p_{PZ} , shown in Figure 6. Past f_R' , capacitors are shorted and L_C' is open, so Z_{PZ} is dominated by the series combination of C_{L_C}' and C_{L_0}' in parallel with C_{PZ} :

$$Z_{PZ}|_{f_0 > f_R'} \approx \frac{1}{sC_{HF}} = \frac{1}{s[(C_{L_C}' \oplus C_{L_0}') + C_{PZ}]}. \quad (14)$$

Note that f_R' and Q_R' depend on C_{PZ} . Specifically, C_{PZ} affects C_{L_C}' (or L_{TC}), indicating that it directly alters the spring's mechanical stiffness [9]. f_R and Q_R , however, are independent of the ED.

Z_{PZ} 's response across frequency is shown in Figure 6, but note that each attribute of the response is variable. f_R and f_R' will be more separated at large k_{CL} and come closer together as k_{CL} reduces. As C_{PZ} gets larger relative to C_{L_0}' and C_{L_C}' , it will dominate the response, and the prominence (i.e., quality factors) of and spacing (i.e., k_F , shown in (11)) between the f_R and f_R' peaks will reduce. When f_R and f_R' get too close together, Z_{PZ} 's peaks may no longer correspond to f_R and f_R' .

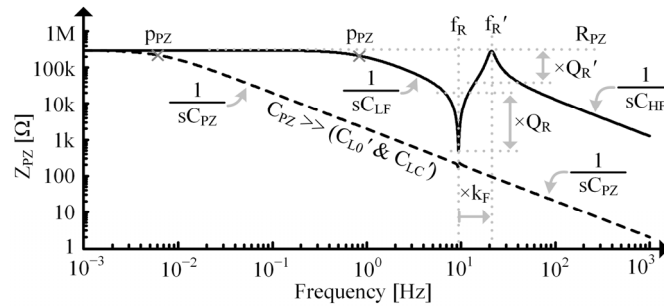


Figure 6. Simulated impedance vs. frequency for a single tone PT on a logarithmic scale.

If C_{PZ} is very small relative to C_{L_0}' and C_{L_C}' , Q and k_F will increase until limited by other factors such as mechanical impedances, k_T , and k_{CL} , and f_R' 's expression reduces to:

$$f_R'|_{C_{PZ} \ll (C_{L_C}' \& C_{L_0}')} \approx \frac{1}{2\pi\sqrt{L_C' C_{L_0}'}} = \frac{1}{2\pi\sqrt{C_T L_T (1 - k_{CL})}}. \quad (15)$$

Using (15), k_{CL} can be approximated as:

$$k_{CL}|_{C_{PZ} \ll (C_{L_C}' \& C_{L_0}')} \approx 1 - \left(\frac{f_R}{f_R'}\right)^2 = 1 - \left(\sqrt{1 - k_{CL}}\right)^2, \quad (16)$$

which is sometimes used for PZ resonators [25,29]. This is useful but may not be applicable in many other contexts as the condition may not be satisfied.

The Norton and Thevenin impedances of Figures 3 and 4 are equal to Z_{PZ} . The Norton equivalent current source, i_{NO} , is equal to the current through a short circuit (SC) across the output, v_{PZ} , which in this case, is equal to the current through C_{L_C}' [28]. With the output shorted, L_C' , R_R' , and C_L' are in series. Using the translations in Section 2.2, the current through that series combination is proportional to v_T by k_T :

$$\begin{aligned} i_{NO} = i_{PZ(SC)} &= \left(\frac{v_S}{Z_{I(SC)}}\right) \left(\frac{C_{L_C}'}{C_{L_C}' + C_{L_0}'}\right) = k_T v_{T(SC)} k_{CL} \\ &= \left(\frac{i_S}{k_T}\right) \left[\frac{1}{R_R' + sL_C' + \left(\frac{1}{sC_{L_C}'} \parallel \frac{1}{sC_{L_0}'}\right)} \right] k_{CL}. \end{aligned} \quad (17)$$

The current through C_{L_C}' is a current divided fraction, k_{CL} , of C_L' , as seen in (6). The Thevenin equivalent voltage source is related to i_{NO} and Z_{PZ} :

$$v_{TH} = i_{NO} Z_{PZ}. \quad (18)$$

2.4. Additional Resonant Tones

A PT can resonate at multiple frequencies depending on its geometry. The shape it deforms into at each resonant frequency is known as a mode of vibration, but in the context of electrical engineering, it adds a tone to the frequency spectrum [30].

Each tone adds resonance in the same way as the fundamental, so adding LCR loops coupled to the ED via transformers accounts for them, as shown in Figure 7. Note that the current/force source in the additional tones is equal to the fundamental's source, and that the mechanical parameters, k_T , and k_{CL} are likely different for each tone [10].

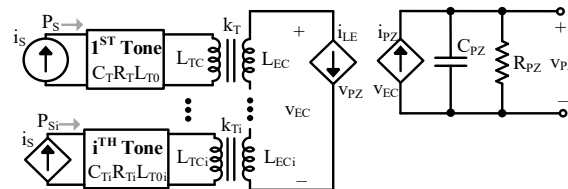


Figure 7. Complete model with additional tones.

While the L_{EC} components of each tone experience the same current, the different k_T s mean different current is induced to each tone. The tones' unique impedances also mean the ac part of i_{LE} affects each tone's voltage differently. When translated, each tone adds an LCR branch which couples to the electrical load via C_{LC}' , as shown in Figure 8. In this case, each branch has the same voltage, but the voltage coupled to each tone is unique because the C_{LC}' s are different.

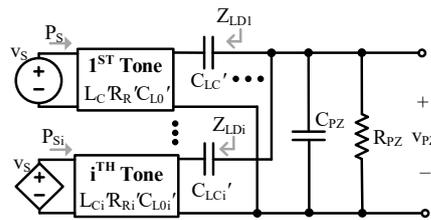


Figure 8. Electrical model with additional tones.

Interestingly, this means that tones add load capacitance relative to other tones. In other words, if looking at a particular tone, i , any tone greater or smaller than i will add to i 's load capacitance, as shown in Figure 9, (20) and (21).

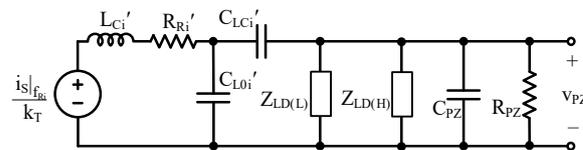


Figure 9. Electrical model of the i th tone with simplified tonal loading.

For tones lower than i , L_{Cn}' is open circuited (OC), so the impedance of those tones is dominated by the series combination of C_{LCn}' and C_{L0n}' of each tone:

$$Z_{LDi} \approx \frac{1}{s(C_{LCi}' \oplus C_{L0i}')} \tag{19}$$

The impedance of each tone appears parallel to each other at the output, so the combined load impedance they contribute is:

$$Z_{LD(L)} = Z_{LD}|_{\text{tones} < i} = Z_{LDi} || \dots || Z_{LD(i-1)} \approx \frac{1}{s \sum_{n=1}^{i-1} (C_{LCn}' \oplus C_{L0n}')} \tag{20}$$

For tones higher than i , L_{Cn}' is a short, so those tones contribute a load impedance, $Z_{LD(H)}$, dominated by C_{LCn}' of each tone:

$$Z_{LD(H)} = Z_{LD}|_{\text{tones} > i} \approx \frac{1}{s \sum_{n=i+1}^{\infty} (C_{LCn})'}. \quad (21)$$

3. Electromechanical Coupling

3.1. Coupling Coefficients

The goal of a PT coupling coefficient is to express the fraction of energy that reaches the ED from the MD (or vice versa). The energy that does not reach the ED is not necessarily lost, as it could remain stored in the MD [31]. To determine the fraction of energy in the MD that reaches the ED, two components of cross-domain energy transfer need to be discussed. First is the fraction of mechanical energy that is available to the ED. The second arises from the fact that only a fraction of that available energy can be captured and used by the ED.

The fraction of mechanical energy available to the ED is directly related to k_{CL} since it represents the PT's inherent ability to convert energy between domains. To capture energy in the ED, though, an electrical load, such as C_{PZ} , needs to be present, but this reduces the fraction of energy available to the ED since impedance is added to the coupling network [31]. In other words, k_{CL} is effectively reduced in the presence of an electrical load. In Figure 4, the series combination of C_{PZ} and C_{LC}' forms a current divider with C_{L0}' , so only a fraction of the power entering the capacitor network, P_{LT} , reaches the EM branch, P_{EM} , thus less mechanical energy is available to the ED. This effect is captured by the mechanical coupling coefficient:

$$k_{CM} = \frac{i_{EC}}{i_{VS}} = \frac{\frac{1}{sC_{L0}'}}{\frac{1}{sC_{L0}'} + Z_{EQ}} = \frac{\frac{1}{sC_{L0}'}}{\frac{1}{sC_{L0}'} + \left[\frac{1}{sC_{LC}'} + \left(\frac{1}{sC_{PZ}} \parallel R_{PZ} \right) \right]}. \quad (22)$$

Mechanically, C_{PZ} effectively increases the spring's stiffness (i.e., reduces L_{TC}), reducing the energy it can store for a given force packet, meaning less is available for coupling [9,31]. k_{CM} is less than or equal to k_{CL} .

When OC, the energy stored in C_{PZ} can be considered as having reached the ED since this is energy that the ED can use. Because L_{TC} is finite, the transformer in Figure 3 requires some energy to transform voltage when loaded. This energy does not reach the ED, but is also not lost, it simply remains in the MD [26]. In Figure 4, C_{PZ} forms a voltage divider with C_{LC}' , so only a fraction of P_{EM} reaches C_{PZ} . In other words, some energy remains in C_{LC}' and does not reach C_{PZ} . This effect is captured with the electrical coupling coefficient:

$$k_{CE} = \frac{v_{PZ}}{v_{LT}} = \frac{Z_{PZ}'}{\frac{1}{sC_{LC}'} + Z_{PZ}'} = \frac{\frac{1}{sC_{PZ}} \parallel R_{PZ}}{\frac{1}{sC_{LC}'} + \left(\frac{1}{sC_{PZ}} \parallel R_{PZ} \right)}, \quad (23)$$

which ideally equals 1. Mechanically, this occurs because the coupled portion of the spring's stiffness is shared between the MD and ED, so an applied force will result in energy that is partially stored in the coupled mechanical spring, L_{TC} , and partially in the "electrical spring", C_{PZ} [9].

k_{CL} represents the *maximum* fraction of mechanical energy available to the ED. k_{CM} pertains to what fraction of that maximum mechanical energy is *actually* available to the ED when a load is present. k_{CE} pertains to what fraction of the available energy is captured by the ED. Note that k_{CM} and k_{CE} are load dependent. The product of these two is the fraction of mechanical energy that is useable/harvestable in the ED and is referred to here as the PT coupling coefficient:

$$k_C = \frac{P_{EC}}{P_{LT}} = k_{CM}k_{CE}. \quad (24)$$

Theoretically, k_C cannot be larger than k_{CL} , regardless of loading conditions, as k_{CL} is a material limit.

3.2. Coupling Extremes

As k_{CL} decreases, it is harder for actions in the ED to affect motion (i.e., it takes a higher v_{PZ} to affect v_{LT}). From this perspective, a small k_{CL} implies a "weakly coupled" PT. This is not to say, though, that the ED cannot have significant effects on motion when k_{CL} is low. If C_{PZ} is small enough, even a small i_{EC} can produce a large v_{PZ} . It is important

to note that coupling effects are ultimately determined by the combined effects of L_T , k_{CL} , and k_T^2 relative to the electrical load. Therefore, a small k_C , which accounts for all those parameters, always means the PT is weakly coupled.

If C_{LC}' is very small, it becomes more difficult for energy to reach the ED because C_{PZ} would need to be significantly smaller for k_{CE} to approach 1 (assuming C_{PZ} is the only electrical load). When k_{CE} approaches 0, only a small fraction of energy is shared between domains, so the MD and ED are essentially disconnected. A very small k_{CL} , though, does not necessarily mean that C_{LC}' is small, as it is also a function of L_T and k_T^2 . k_{CE} approaching 0, however, always means C_{LC}' is much smaller than C_{PZ} , so:

$$Z_{PZ}|^{k_{CE} \rightarrow 0} \rightarrow \frac{1}{sC_{PZ}} || R_{PZ}. \quad (25)$$

In other words, C_{PZ} effectively shorts the MD. Since capacitance typically corresponds to large impedances at frequencies of interest for energy harvesting, a Norton equivalent is preferred to model this extreme. This is often performed in the SoA by saying the PT is “weakly coupled” without much further justification, but now (23) and (25) can be used definitively [1,4,7,16–20]. Note that PTs traditionally considered weakly coupled may not actually fulfill this approximation. Note also, that changing the load could change the applicability of the approximation.

If k_{CL} approaches 1, the MD becomes fully connected to the ED, so Z_{PZ} includes f_R and f_R' . k_{CM} approaching 1 means the same thing but also implies C_{PZ} is much bigger than C_{LC}' and C_{L0}' . At f_R , L_C' and C_{LC}' effectively short and C_{L0}' opens, so:

$$Z_{PZ}|_{f_R}^{k_C \rightarrow 1} \rightarrow R_R' || R_{PZ} \approx R_R', \quad (26)$$

since R_{PZ} is typically big. R_R' is usually small, so for these cases, a Thevenin equivalent would be preferred. At f_R' , the resonant network exhibits a huge impedance parallel to R_{PZ} , so:

$$Z_{PZ}|_{f_R'}^{k_C \rightarrow 1} \rightarrow R_{PZ}. \quad (27)$$

Since R_{PZ} is normally large, this case is also best modeled with a Norton equivalent.

3.3. Coupling with a Capacitive Load

When a PT is loaded with a capacitor, C_{LD} , such that the total output capacitance, C_O , is:

$$C_O = C_{PZ} + C_{LD}, \quad (28)$$

and assuming R_{PZ} is very large, an interesting tradeoff exists between k_{CM} and k_{CE} . To maximize k_{CM} , C_O should be much larger than C_{LC}' and C_{L0}' , but to maximize k_{CE} , C_O should be much smaller than C_{LC}' and C_{L0}' . So, if k_{CM} is maximized, k_{CE} , and therefore k_C , go to 0, and vice versa. This implies an optimal C_O exists to maximize k_C , $C_{O(MKC)}$.

Using (21)–(24) and approximating R_{PZ} as large, an expression for k_C with respect to C_O can be made:

$$k_C|_{f_R'} \approx \frac{(C_{LC}' \oplus C_O)C_{LC}'}{[C_{L0}' + (C_{LC}' \oplus C_O)](C_{LC}' + C_O)}. \quad (29)$$

k_C is evaluated at f_R' as this is the frequency at which the maximum voltage occurs and the frequency the beam freely vibrates at. To find $C_{O(MKC)}$, the derivative of (29) with respect to C_O is equated to 0:

$$\frac{dk_C}{dC_O} \approx - \left(\frac{C_{LC}'^2 (C_{L0}' C_O^2 - C_{LC}'^2 C_{L0}')}{(C_O + C_{LC}')^2 (C_{L0}' C_O + C_{L0}' C_{LC}')^2} \right) \equiv 0. \quad (30)$$

Solving for C_O in (30) gives the optimal C_O to maximize k_C for a particular k_{CL} :

$$C_{O(MKC)} \approx C_{LC}' \sqrt{\frac{C_{L0}'}{C_{L0}'}} = C_{L0}' k_{CL} \sqrt{1 - k_{CL}}. \quad (31)$$

Plugging (31) back into (29) gives an expression for the maximum PT coupling coefficient that can be achieved for a PT, $k_{C(\text{MAX})}$, with a particular k_{CL} and capacitive load:

$$k_{C(\text{MAX})} = k_C|_{C_{O(\text{MKC})}} \approx \left(\frac{\sqrt{k_{CL}}}{1 + \sqrt{1 - k_{CL}}} \right)^2. \quad (32)$$

This highlights the difference between a PT's intrinsic ability to couple between domains, k_{CL} , and the fraction of energy that can be practically captured in the ED, k_C . It also highlights the effect electrical loading can have on available electrical energy, since in this case, $k_{C(\text{MAX})}$ is always less than k_{CL} , unless k_{CL} equals 1. The $k_{C(\text{MAX})}$ line for a given k_{CL} can be seen in Figure 10. If C_O is larger than $C_{O(\text{MKC})}$, then the PT's motion is increased, so more energy is available, but the ability to capture that energy in the ED is decreased, underdamping the system. If C_O is smaller than $C_{O(\text{MKC})}$, the ability to capture energy in the ED is increased, but mechanical motion is decreased, overdamping the system. Optimizing k_C will always improve electrical energy capture, but as k_{CL} becomes very small (much less than 1% for example), the conditions required to achieve optimization could become impractical.

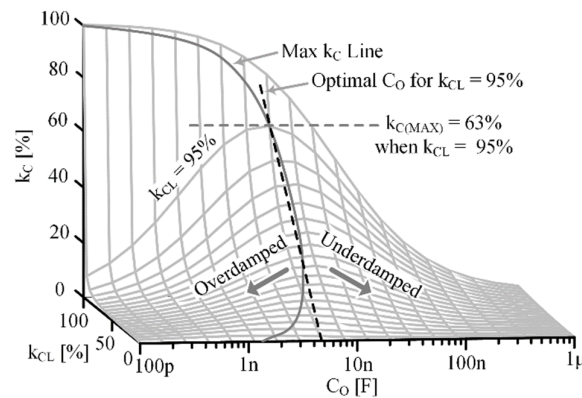


Figure 10. Simulated k_C at various k_{CL} and C_O combinations.

4. Parameter Extraction

The model and analysis presented in the previous sections are applicable to many PT types and dimensions, as discussed in Section 2.1. This section describes a method for extracting each parameter of the model specifically from a real cantilever-style PT with a tip mass to illustrate a way to use the model practically. The methods can be expanded upon in future work to develop extraction methods for other types of PTs and contexts. The method begins by assuming a single-tone PT and then provides techniques for accounting for higher tones.

4.1. Mechanical Parameters

The mechanical parameters are arguably the simplest to extract, so they are determined first. If the PT's tip mass, M_T , is much larger than the PT's mass, then [22,23]:

$$C_T = M_T. \quad (33)$$

Therefore, C_T can be determined by weighing the tip mass. Since the PT and mass form a spring-mass resonator, L_T is related to C_T by f_R . To measure f_R , SC the PT's output so the ED is not loading the MD and measure the period of d_x and/or v_T of an initially displaced beam using a displacement sensor, as shown in Figure 11. Measuring the response of an initially displaced beam allows the PT to resonate freely at its f_R .

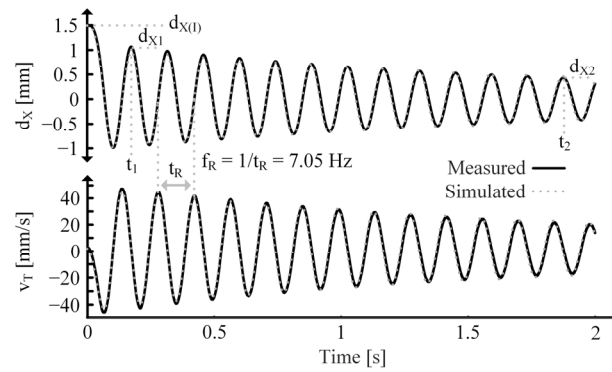


Figure 11. Measured/simulated d_X and v_T for initially displaced SC PT.

C_T and f_R can then be used to determine L_T :

$$L_T = \left(\frac{1}{2\pi f_R} \right)^2 \left(\frac{1}{C_T} \right) = \left(\frac{t_R}{2\pi} \right)^2 \left(\frac{1}{C_T} \right). \quad (34)$$

The PT-mass system exhibits damped resonance, so its behavior is of the form:

$$i_{LT} = \frac{d_X}{L_T} = i_{LT(1)} e^{-\left(\frac{t}{2R_T C_T}\right)}, \quad (35)$$

where $i_{LT(1)}$ represents the initial force in the spring resulting from the initial displacement, $d_{X(1)}$. By choosing two different points along the d_X curve, such as (d_{X1}, t_1) and (d_{X2}, t_2) as shown in Figure 11, two different instances of (35) are determined. Taking the ratio of these instances and rearranging the expression to isolate R_T results in:

$$R_T = \frac{t_2 - t_1}{2C_T \ln\left(\frac{d_{X1}}{d_{X2}}\right)}. \quad (36)$$

4.2. Electrical Parameters

Extracting the electrical parameters is a little more involved. Recall from Section 2.3 that past f_R' , L_C' is open, so the measured impedance, Z_O , at these frequencies would be:

$$\begin{aligned} Z_O|_{f_0 \gg f_R'} &\approx \frac{1}{sC_{HF}} = \frac{1}{sC_{PZ}} \parallel \frac{1}{s(C_{LC} \oplus C_{L0}')} \\ &= \frac{1}{sC_{PZ}} \parallel \frac{1}{s(L_T k_{CL}(1 - k_{CL})k_T^2)}. \end{aligned} \quad (37)$$

Note that C_{PZ} cannot be measured directly, but C_{HF} can be.

There are two main challenges with using an impedance analyzer (IA) to determine R_{PZ} : output impedance and minimum frequency. R_{PZ} is typically very large (on the order of $M\Omega$), so the IA's output impedance needs to be larger than that to give an accurate measure of R_{PZ} . Plus, since R_{PZ} is so large, p_{PZ} typically occurs around or below 1 Hz, so the IA needs to operate at those frequencies to provide a measurement of R_{PZ} . If an IA is on hand which satisfies these requirements, that is the best method for determining R_{PZ} . If such an IA is not accessible, the PT's discharge rate, shown in Figure 12, can be used since a PT's output is largely capacitive.

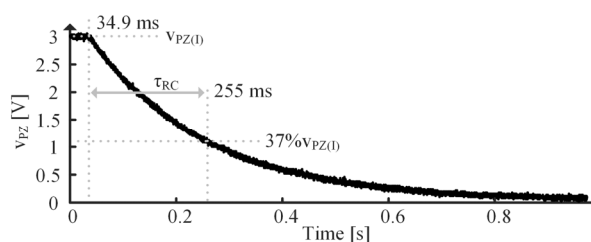


Figure 12. Measured discharge of immobilized PT.

Begin by immobilizing the beam—this ensures Z_O is dominated by C_{HF} across all frequencies greater than p_{PZ} by forcing v_T to 0. Then connect the PT to a power supply set to a particular voltage and allow it to charge. Disconnect the PT from the supply and measure the voltage across the PT's terminals, v_{PZ} , with an oscilloscope. The time it takes for the voltage to drop from the initial voltage, $v_{PZ(I)}$, to 37% of $v_{PZ(I)}$ is one time constant, τ_{RC} . R_{PZ} can be determined using:

$$R_{PZ} = \frac{\tau_{RC}}{C_{HF}}. \quad (38)$$

Rearranging (37) and substituting in (17) for k_T gives an expression for C_{PZ} :

$$C_{PZ} = C_{HF} - L_T \left(\frac{1 - k_{CL}}{k_{CL}} \right) \left(\frac{i_{PZ,PK(SC)}}{v_{T,PK(SC)}} \right)^2, \quad (39)$$

where $i_{PZ,PK(SC)}$ is the measured, peak, SC current corresponding to a particular measured, peak, SC velocity, $v_{T,PK(SC)}$. $v_{T,PK(SC)}$ can be measured using a d_x sensor. There are two unknowns in (39): C_{PZ} and k_{CL} , but it is known that k_{CL} is between 0 and 1. To determine C_{PZ} and k_{CL} , software aided curve fitting is performed on the OC v_{PZ} , shown in Figure 13. Curve fitting computes a selection of variables to yield the least error within given boundary conditions [32,33]. (39) is used as a boundary condition to ensure the results apply to the PT. (39) and $v_{PZ(OC)}$ curve fitting essentially act as two equations to solve for the two unknowns: C_{PZ} and k_{CL} . Only k_{CL} is adjusted during fitting since all other parameters have been determined, and because the bounds are well defined, there should only be one unique solution. After k_{CL} is determined from the fit, it is plugged into (39) to find C_{PZ} . k_T can then be found with (17) using k_{CL} , $i_{PZ,PK(SC)}$ and $v_{T,PK(SC)}$.

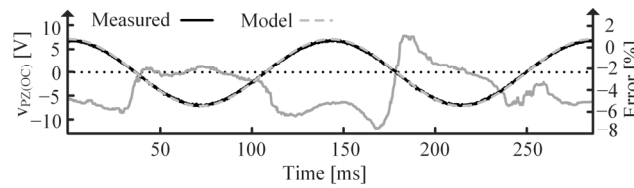


Figure 13. Measured $v_{PZ(OC)}$ and modeled $v_{PZ(OC)}$ after curve fitting with resulting percent error.

The relationship between k_{CL} and L_T is described in Section 2.1. To restate, k_{CL} can be used to determine L_{TC} with:

$$L_{TC} = L_T k_{CL}, \quad (40)$$

and L_{T0} with:

$$L_{T0} = L_T - L_{TC} = L_T(1 - k_{CL}). \quad (41)$$

4.3. Approximating 2nd Tone

As discussed in Section 2.4, higher tones can affect PT behavior, so it can be important to account for them. Approximating the second tone is discussed here, but the methods could be extended to higher tones. Unfortunately, it is difficult to extract these parameters since C_{T2} is not equal to M_T .

If operating the PT with a constant applied force of frequency f'_R , no energy is supplied by the higher tones, so they simply act as capacitive loads. In this case, use C_{HF1} , shown in Figure 14, in (39). This way, C_{PZ} will include the capacitive effects contributed by the higher tones, providing the correct loading with respect to the MD but overestimating the ED's energy storage capacity.

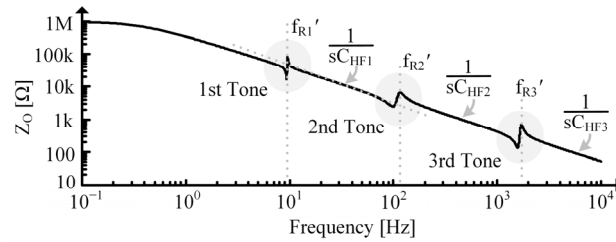


Figure 14. Simulated Z_O for multi-tone PT to show C_{HF} measurements.

If working with a step function input, the higher tones supply energy to the ED, so it is ideal to account for their full models. While f_{R2}' can be measured, C_{T2} is unknown, so L_{T2} cannot be determined. C_{HF2} and $i_{PZ,PK(SC)}$ can also be measured, but $v_{T,PK(SC)}$ can be difficult to measure since a high-speed, high-sensitivity displacement sensor is required. So, to approximate R_{T2} , C_{T2} , L_{T2} , k_{T2} , and k_{CL2} , parameter estimation/curve fitting can be used [32,33]. C_{PZ} has a similar limiting condition as before, but this time, the first tone capacitance is accounted for, and more is unknown:

$$C_{PZ} = C_{HF2} - (C_{LC1}' \oplus C_{L01}') - L_{T2} \left(\frac{1 - k_{CL2}}{k_{CL2}} \right) \left(\frac{i_{PZ,PK(SC)}}{v_{T,PK(SC)}} \right)^2. \quad (42)$$

Note that while curve fitting here should provide a good approximation of the effects of the second tone, since so many variables are being fitted and the limiting conditions are not as rigorous or as well-defined as for the first tone, the resulting second tone parameters may not necessarily correspond to the actual device parameters, and it is possible that there could be more than one unique solution. However, if there is a relationship between C_{T2} and M_T and a good d_X sensor is on hand, extraction could be performed like what is described in A and B.

5. Model Validation

5.1. Test Setup

To validate the model described in Section 2, the methods described in Section 4 are performed on the MIDE S129 PT to extract its model parameters using the test setup shown in Figure 15. SPICE simulations are then performed on the model with extracted parameters and the results are compared with measured data.

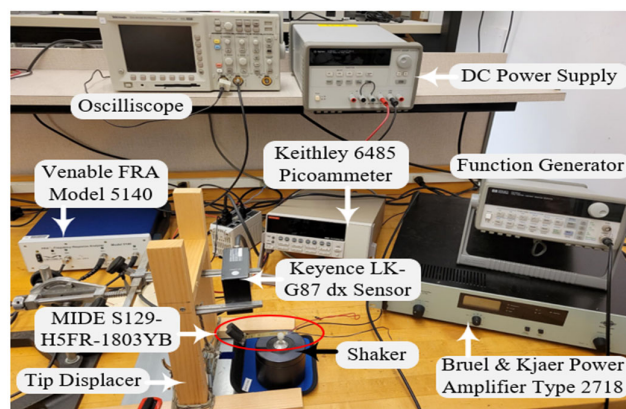


Figure 15. Test setup.

The PT is mounted on a Bruel & Kjaer shaker with a 36 g weight attached to its tip. The frequency response analyzer (FRA) is used as the IA. The picoammeter is used to measure i_{EC} and to SC the PT. The oscilloscope measures v_{PZ} . The PT is $2.795 \times 0.407 \times 0.029$ in.

5.2. Parameter Extraction

The MIDE S129 PT only weighs about 1.4 g, so with a 36 g tip mass, (33) holds true. So, C_T is 36 mF (“milli” is used because the SI unit of mass is kg). d_X of the PT tip is measured using the Keyence d_X sensor shown in Figure 15. While shorted, the PT is bent to an initial displacement, released, and allowed to vibrate freely. Figure 11 shows the measured d_X and v_T , for the PT which is used to extract L_T and R_T .

R_{PZ} is determined using τ_{PZ} measured in Figure 12 and the immobilized capacitance of the PT. The PT is immobilized by clamping it to a table and is charged using the power supply shown in Figure 15. The discharge is measured using the oscilloscope in Figure 15. Since the MIDE S129 with a 36 g tip mass has multiple tones, as seen in Figure 16, C_{HF1} is used in (39) and C_{HF2} is used when approximating the second tone parameters. Recall from Section 4.3, though, that using C_{HF1} in (39) means the extracted C_{PZ} includes capacitive loading effects from the higher tones in Figure 16.

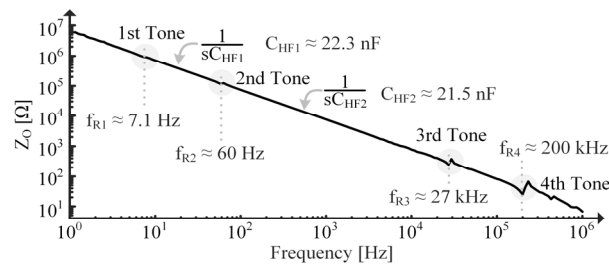


Figure 16. Measured Z_O vs. frequency of MIDE S129 with 36 g tip mass using FRA.

The measured $i_{PZ,PK(SC)}$ and $v_{T,PK(SC)}$ are shown in Figure 17. All variables required for (39) have now been measured and/or determined, so curve fitting can commence. The results of the curve fit are shown in Figure 13. All extracted model parameters are shown in Table 1. Plugging these into (23), k_{CE} for this PT loaded by its C_{PZ} is 10%, which is not small enough to assume it is weakly coupled, as (25) shows (k_{CE} would need to be much less than 1%), contrary to what would be performed in the SoA.

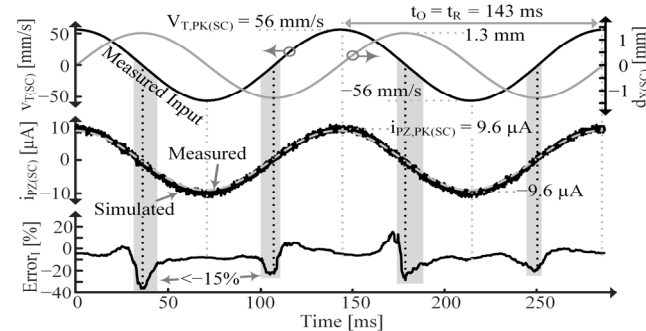


Figure 17. Measured $v_{T(SC)}$, $d_X(SC)$, and $i_{PZ(SC)}$ and simulated $i_{PZ(SC)}$ for constantly vibrating PT and average percent error.

Table 1. Extracted Parameters.

Variable	Value
C_T	36.0 mF
L_T	13.9 mH
R_T	32.3 Ω
k_{CL}	16.4%
k_T	993 $\mu \frac{Vs}{m}$
C_{PZ}	20.4 nF
R_{PZ}	11.3 M Ω
f_{R2}	60 Hz

5.3. Resonant Vibrations

In this section, the PT’s response to a constant applied vibration at f_R' is considered and compared to simulated model results. In this case, the force source, i_S , is not known, but $v_{T(SC)}$ is, so the Norton model shown in Figure 5 is used for simulations.

Consider first the SC case, shown in Figure 17, where measured and simulated i_{PZ} are compared. The error between simulated and measured data is found with:

$$\text{Error} = \frac{\text{Simulated} - \text{Measured}}{\text{Measured}}, \tag{43}$$

and its average is plotted at the bottom of Figure 17. The areas highlighted in gray indicate where percent error exceeds $\pm 15\%$. Note that error spikes every time i_{PZ} crosses 0 because if measured data equals 0 and simulated data do not (which happens with the smallest difference in period), error spikes to infinity.

Figure 18 shows simulated and measured data for the OC PT. Note the difference in period, t_R and t_R' , between the SC and OC cases, respectively, which results from C_{PZ} ’s inclusion when OC, as discussed in Section 2.3 [9]. t_R' is the period of an f_R' vibration. Also note that i_{PZ} is in phase with v_T while v_{PZ} is in phase with d_X [1,4,7,9,16–20]. Error_v is smaller than Error_i because $v_{PZ(OC)}$ is used for curve fitting, so any parameter errors will be more apparent in the $i_{PZ(SC)}$ plots.

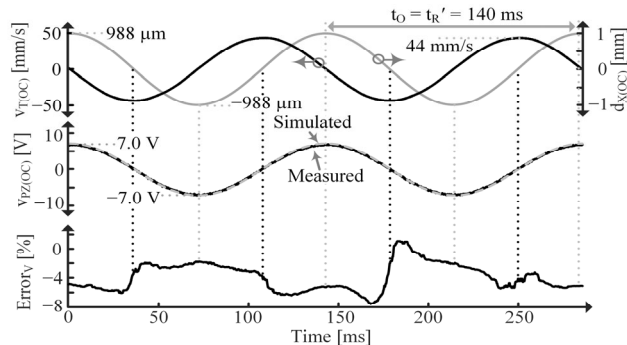


Figure 18. Measured $v_{T(OC)}$, $d_{X(OC)}$ and $v_{PZ(OC)}$ and simulated $v_{PZ(OC)}$ for constantly vibrating PT and average percent error.

In Figure 19, resistors are applied across the PT to test the model’s ability to predict accurate responses under various loading conditions. Energy burned by a load resistor, E_R , is measured across a one-second time interval when the PT experiences the same $v_{T(SC)}$ as in Figure 17. Figure 19 estimates the maximum power point (MPP) resistance to be about the same as what was measured and shows approximately a 9% error between the MPP energies, $E_{R(MPP)}$. Deviations between simulated and measured data at very low R_{LOAD} are attributed to the noise floor limits of the oscilloscope. Similarly, deviation at high R_{LOAD} is most likely due to the limitation of the ammeter.

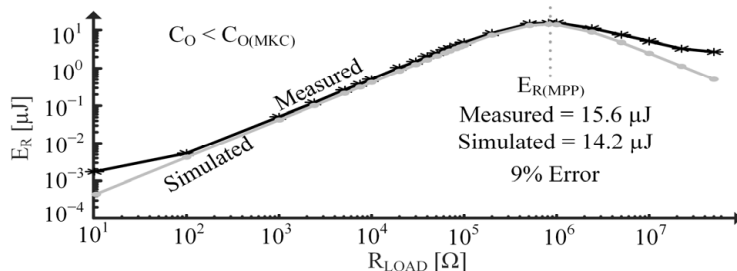


Figure 19. Measured/simulated E_R vs. load for constantly vibrating PT.

Error between simulated and measured response likely comes largely from errors in measurements used for parameter extraction. Measuring C_{HF1} , for example, can be

difficult since it is flanked by resonances, so the impedance line is slightly variable. Small rounding differences when measuring f_R can also lead to large error differences since it is squared when calculating L_T . Certain assumptions/approximations made during parameter extraction, such as neglecting the PT's mass and approximating impedance as purely capacitive at C_{HF1} can also contribute error. Errors introduced by measurement equipment, such as quantization noise and electronic noise, and the test setup, such as parasitics, can also add to total error.

5.4. Step Response

This section discusses the PT's response to a step input. The PT is bent and clamped to have an initial displacement, then released to resonate freely. This can be modeled in Figure 3 as i_S having a constant, non-zero value long enough for the system to reach steady state. At steady state, all the current (force) goes through L_T (the spring), which models the PT's spring storing energy while displaced. To model releasing the PT, drop i_S to 0 very quickly. Note this is not a perfect step response as that would require an instantaneous beam release. Instead, there is some "ramp" as i_S drops to 0 in a finite amount of time.

Since the input is approximately a step function, it is ideal to model higher tones. Table 2 shows the approximated 2nd tone parameters found using methods described in Section 4.3. Remember from Section 4.3 that these 2nd tone parameters may not correspond to actual device parameters but provide good approximations for device behavior and are included here to demonstrate the model's ability to account for higher tones. C_{PZ} also reduces to 19.6 nF since it no longer includes the second tone's load, per (42). A perfect step function contains many frequencies, but as the step becomes less ideal (i.e., it takes more time to drop to 0), power in the higher frequencies reduces [34]. In this experiment, an ideal beam release was not achieved, so tones higher than the second do not receive enough energy to have significant effects and are thus neglected.

Table 2. Approximated 2nd Tone Parameters.

Variable	Value
C_{T2}	1.0 mF
L_{T2}	6.9 mH
R_{T2}	54.5 Ω
k_{CL2}	45.0%
k_{T2}	133 $\mu \frac{Vs}{m}$

Figure 20 shows the response for the SC PT released from an initial displacement, $d_{X(1)}$, which corresponds to an initial force, $i_{S(1)}$. Note that $i_{S(1)}$ can be determined with (35) because all the current (force) goes through L_T . Since the PT is SC, it oscillates at f_R . The effects of the second tone can also be seen, especially in Figure 20b, and its frequency, f_{R2} , can be measured. The errors with and without the second tone approximation are shown. After the second tone's effects subside, the errors are the same and always less than $\pm 10\%$. However, including the second tone greatly reduces error while its effect is present, indicating the model's ability to accurately account for higher tones.

Figure 21 shows the response for the OC PT released from approximately the same $d_{X(1)}$, but this time the PT oscillates at f_R' since it is OC. Again, the difference in error with and without the second-order approximation is only present for the first few cycles, but it is significant during those cycles. The reason the error seems to decrease with time is most likely a result of slight frequency error. Interestingly, the simulated voltage is higher (more negative) if the second tone is not accounted for (as is corroborated with the $Error_V$ plot). This implies that the second tone drains C_{PZ} , effectively opposing the first tone [9].

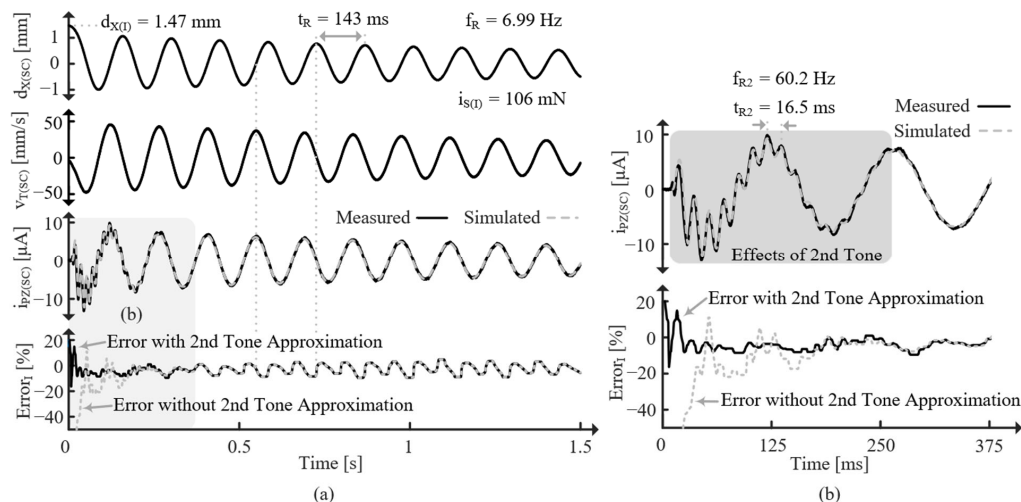


Figure 20. (a) Measured d_x , v_T , and i_{pZ} for initially displaced SC PT and average percent i_{pZ} error compared with simulations. (b) Zoomed in on the gray region of (a).

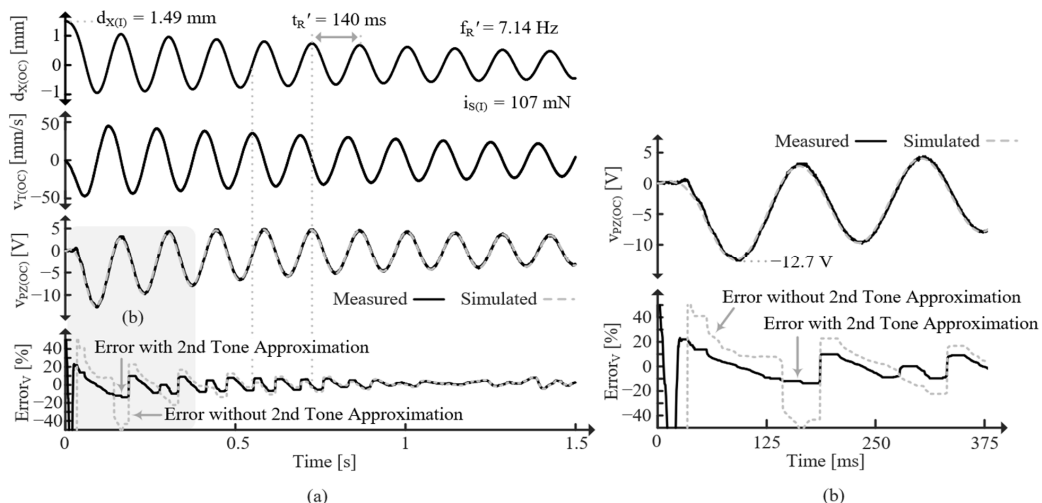


Figure 21. (a) Measured d_x , v_T , and v_{pZ} for initially displaced OC PT and average percent v_{pZ} error compared with simulations. (b) Zoomed in on the gray region of (a).

Figure 22 tests the two-tone model’s ability to predict accurate responses under various loading conditions when the PT is initially displaced. Energy burned by the resistor is measured after the beam has resonated for 9 s with a $d_{x(I)}$ of about 1 mm. The measured and simulated data show good agreement with only about an 8% error and the same MPP R_{LOAD} . Excluding the second tone’s effects yields about a 9% error. This difference is likely small because the 9-s window is much larger than the fraction of a second that the second tone is present. If the input were closer to an ideal step function, though, the difference is expected to be larger.

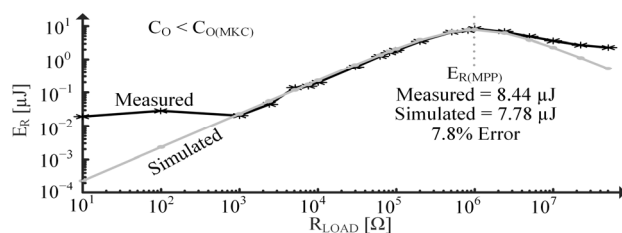


Figure 22. Measured/simulated E_{OUT} vs. load for initially displaced PT.

6. Conclusions

The complete EM model presented here provides insight into PT energy transfers which was not previously possible by explicitly defining PT parameters not previously represented individually nor completely. The model is generally applicable to many PT types and dimensions and does not rely on coupling assumptions, removing guesswork from designing PT interface circuits. L_T is split into its coupled and uncoupled parts, enabling explicit and accurate definition, visualization, and grasp of k_{CL} and k_T . Incorporating L_T into the transformer illustrates its role and related losses in EM energy transfer. Total coupling between domains, limitations to the amount of energy harvestable, and loading effects are shown to be dependent on k_{CL} , k_T^2 , the load, and the PT's stiffness. It is shown that when k_{CE} approaches 0, the model can be reduced to a current source parallel to C_{PZ} (typical for weakly coupled PTs). When k_C approaches 1, a Thevenin equivalent is preferred.

When constant sinusoidal vibrations are applied to a PT, it is shown that the other tones simply load the fundamental, whereas when an irregular vibration is applied, the other tones can oppose or support energy generation. This model also adequately captures a PT's impedance behavior making it useful in many contexts, removing the need to switch to different models for different applications, and, in a sense, unifying concepts of various existing PT models into one complete model.

Parameter extraction methods for cantilever style PTs with a tip mass are presented and performed to illustrate a way to use the model practically. Using the extraction methods, designers can effectively and easily model off-the-shelf PTs, enabling easy integration of PTs into SPICE simulations to assist in harvester or interface circuit development. In most cases, less than 5–10% error is observed between measurements and the model with extracted parameters. The model's ability to capture responses of PTs used as both resonators and energy sources, which are generally accepted in the SoA, further supports it.

The model described here is generalized, but work can be performed to apply it to specific PTs by deriving expressions for each component in Figure 3 in terms of material, dielectric, and piezoelectric constants. Concepts from this paper and [9] and an understanding of transformer turns ratios and mutual inductance can help accomplish this. The resulting expressions would be material and dimension dependent and would provide more insight into the physical parameters contributing to energy generation and loss.

Author Contributions: Conceptualization, M.L.I. and G.A.R.-M.; methodology, M.L.I. and G.A.R.-M.; software, M.L.I.; validation, M.L.I.; formal analysis, M.L.I.; investigation, M.L.I.; resources, G.A.R.-M.; data curation, M.L.I.; writing—original draft preparation, M.L.I.; writing—review and editing, M.L.I. and G.A.R.-M.; visualization, M.L.I. and G.A.R.-M.; supervision, G.A.R.-M.; project administration, G.A.R.-M.; funding acquisition, G.A.R.-M. All authors have read and agreed to the published version of the manuscript.

Funding: This research received no external funding.

Institutional Review Board Statement: Not applicable.

Informed Consent Statement: Not applicable.

Data Availability Statement: Data are contained within the article.

Conflicts of Interest: The authors declare no conflicts of interest.

References

1. Covaci, C.; Gontean, A. Piezoelectric Energy Harvesting Solutions: A Review. *Sensors* **2020**, *20*, 3512. [[CrossRef](#)]
2. Ju, S.; Ji, C. Indirect impact based piezoelectric energy harvester for low frequency vibration. In Proceedings of the 2015 IEEE Transducers—18th International Conference on Solid-State Sensors, Actuators and Microsyst, Anchorage, AK, USA, 21–25 June 2015; pp. 1913–1916.
3. Deterre, M.; Lefeuvre, E.; Zhu, Y.; Woytasik, M.; Boutaud, B.; Molin, R.D. Micro Blood Pressure Energy Harvester for Intracardiac Pacemaker. *J. Microelectromech. Syst.* **2014**, *23*, 651–660. [[CrossRef](#)]

4. Li, H.; Tian, C.; Deng, Z.D. Energy harvesting from low frequency applications using piezoelectric materials. *Appl. Phys. Rev.* **2014**, *1*, 041301. [[CrossRef](#)]
5. Song, H.C.; Kumar, P.; Maurya, D.; Kang, M.G.; Reynolds, W.T.; Jeong, D.Y.; Kang, C.Y.; Priya, S. Ultra-Low Resonant Piezoelectric MEMS Energy Harvester with High Power Density. *J. Microelectromech. Syst.* **2017**, *26*, 1226–1234. [[CrossRef](#)]
6. Li, X.; Rincon-Mora, G.A. Maximum power-point theory for thermoelectric harvesters. In Proceedings of the 2023 IEEE 66th Midwest Symposium on Circuits and Systems, Tempe, AZ, USA, 6–9 August 2023; pp. 409–413.
7. Rincón-Mora, G.A.; Yang, S. Tiny piezoelectric harvesters: Principles, constraints, and power conversion. *IEEE Trans. Circ. Syst. I* **2016**, *63*, 639–649. [[CrossRef](#)]
8. Guyomar, D.; Badel, A.; Lefeuvre, E.; Richard, C. Toward energy harvesting using active materials and conversion improvement by nonlinear processing. *IEEE Trans. Ultrason. Ferroelectr. Freq. Control* **2005**, *52*, 584–595. [[CrossRef](#)]
9. Erturk, A.; Inman, D.J. A distributed parameter electromechanical model for Cantilevered Piezoelectric Energy Harvesters. *J. Vib. Acoust.* **2008**, *130*, 041002. [[CrossRef](#)]
10. Elvin, N.G.; Elvin, A.A. A general equivalent circuit model for piezoelectric generators. *J. Intell. Mater. Syst. Struct.* **2008**, *20*, 3–9. [[CrossRef](#)]
11. Yang, Y.; Tang, L. Equivalent Circuit Modeling of Piezoelectric Energy Harvesters. *J. Intell. Mater. Syst. Struct.* **2009**, *20*, 2223–2235. [[CrossRef](#)]
12. Pollet, B.; Despesse, G.; Costa, F. A New Non-Isolated Low-Power Inductorless Piezoelectric DC–DC Converter. *IEEE Trans. Power Electron.* **2019**, *34*, 11002–11013. [[CrossRef](#)]
13. Boles, J.D.; Piel, J.J.; Perreault, D.J. Enumeration and Analysis of DC–DC Converter Implementations Based on Piezoelectric Resonators. *IEEE Trans. Power Electron.* **2021**, *36*, 129–145. [[CrossRef](#)]
14. Pereira, L.d.A.; Morel, A.; Touhami, M.; Lamorelle, T.; Despesse, G.; Pillonnet, G. Operating Frequency Prediction of Piezoelectric DC–DC Converters. *IEEE Trans. Power Electron.* **2022**, *37*, 2508–2512. [[CrossRef](#)]
15. Boles, J.D.; Bonavia, J.E.; Lang, J.H.; Perreault, D.J. A Piezoelectric-Resonator-Based DC–DC Converter Demonstrating 1 kW/cm Resonator Power Density. *IEEE Trans. Power Electron.* **2023**, *38*, 2811–2815. [[CrossRef](#)]
16. Edla, M.; Lim, Y.Y.; Mikio, D.; Padilla, R.V. A Single-Stage Rectifier-Less Boost Converter Circuit for Piezoelectric Energy Harvesting Systems. *IEEE Trans. Energy Convers.* **2022**, *37*, 505–514. [[CrossRef](#)]
17. Oh, T.; Islam, S.K.; To, G.; Mahfouz, M. Powering wearable sensors with a low-power CMOS piezoelectric energy harvesting circuit. In Proceedings of the 2017 IEEE International Symposium on Medical Measurements and Applications, Rochester, MN, USA, 7–10 May 2017; pp. 308–313.
18. Yang, S.; Rincón-Mora, G.A. Energy-Harvesting Piezoelectric-Powered CMOS Series Switched-Inductor Bridge. *IEEE Trans. Power Electron.* **2019**, *34*, 6489–6497. [[CrossRef](#)]
19. Yang, S.; Rincón-Mora, G.A. Efficient Power Transfers in Piezoelectric Energy-Harvesting Switched-Inductor Chargers. *IEEE Trans. Circuits Syst. II Express Briefs* **2021**, *68*, 1248–1252. [[CrossRef](#)]
20. Roy, S.; Azad, A.N.M.W.; Baidya, S.; Khan, F. A Comprehensive Review on Rectifiers, Linear Regulators, and Switched-Mode Power Processing Techniques for Biomedical Sensors and Implants Utilizing in-Body Energy Harvesting and External Power Delivery. *IEEE Trans. Power Electron.* **2021**, *36*, 12721–12745. [[CrossRef](#)]
21. Van Dyke, K.S. The Piezo-Electric Resonator and Its Equivalent Network. *Proc. Inst. Radio Eng.* **1928**, *16*, 742–764. [[CrossRef](#)]
22. Friswell, M.I.; Ali, S.F.; Bilgen, O.; Adhikari, S.; Lees, A.W.; Litak, G. Non-linear piezoelectric vibration energy harvesting from a vertical cantilever beam with tip mass. *J. Intell. Mater. Syst. Struct.* **2012**, *23*, 1505–1521. [[CrossRef](#)]
23. Hongjin, W.; Qingfeng, M.; Wuwei, F. Discussion of the Improved Methods for Analyzing a Cantilever Beam Carrying a Tip-Mass under Base Excitation. *Shock Vib.* **2014**, *2014*, 981053. [[CrossRef](#)]
24. Isaf, M.L.; Rincon-Mora, G.A. Piezoelectric transducers for energy harvesting: Electromechanical model, ambient motion, and electrical loads. In Proceedings of the 2022 29th IEEE International Conference on Electronics, Circuits and Systems, Glasgow, UK, 24–26 October 2022; pp. 1–4.
25. Arnau, A.; Soares, D. Fundamentals of Piezoelectricity. In *Piezoelectric Transducers and Applications*; Vives, A.A., Ed.; Springer: Berlin/Heidelberg, Germany, 2009.
26. Shaarbafi, K. *Transformer Modelling Guide*; Teshmont Consultants LP: Winnipeg, MB, Canada, 2014.
27. Kim, S.B.; Park, J.H.; Kim, S.H.; Ahn, H.; Wickle, H.C.; Kim, D.J. Modeling and Evaluation of d33 Mode Piezoelectric Energy Harvesters. *J. Micromech. Microeng.* **2012**, *22*, 105013. [[CrossRef](#)]
28. Rincon-Mora, G.A. *Switched Inductor Power IC Design*; Springer Nature: New York, NY, USA, 2022.
29. Kim, S.-B.; Park, H.; Kim, S.-H.; Wickle, H.C.; Park, J.-H.; Kim, D.-J. Comparison of MEMS PT Cantilevers Based on d31 and d33 Modes for Vibration Energy Harvesting. *J. Microelectromech. Syst.* **2013**, *22*, 26–33. [[CrossRef](#)]
30. Ewins, D.J. Mode of Vibration. In *Encyclopedia of Vibration*; Elsevier: Amsterdam, The Netherlands, 2001; pp. 838–844.
31. Lustig, S.; Elata, D. Ambiguous definitions of the piezoelectric coupling factor. *J. Intell. Mater. Syst. Struct.* **2020**, *31*, 1689–1696. [[CrossRef](#)]
32. Kirkham, H.; Riepnies, A. Students' simple method for determining the parameters of an AC signal. In Proceedings of the 2016 57th International Scientific Conference on Power and Electrical Engineering of Riga Tech University, Riga, Latvia, 13–14 October 2016.

-
33. Alhanaty, M.; Bercovier, M. Curve fitting and design by optimal control methods. In Proceedings of the 1998 IEEE Conference on Information Visualization, London, UK, 31 July 1998.
 34. Close, C.M. *Modelling and Analysis of Dynamic Systems*; Houghton Mifflin Company: Boston, MA, USA, 1993.

Disclaimer/Publisher's Note: The statements, opinions and data contained in all publications are solely those of the individual author(s) and contributor(s) and not of MDPI and/or the editor(s). MDPI and/or the editor(s) disclaim responsibility for any injury to people or property resulting from any ideas, methods, instructions or products referred to in the content.